Materials Advances

Accepted Manuscript

This article can be cited before page numbers have been issued, to do this please use: S. Annurakshita, M. Kellomäki and V. S. Parihar, *Mater. Adv.*, 2026, DOI: 10.1039/D6MA00668J.

ROYAL SOCIETY OF CHEMISTRY

rsc.li/materials-advances

Photocrosslinkable graphene-enhanced biomaterial inks for improved printability and structural fidelity

View Article Online
DOI: 10.1039/D6MA00668J

Shambhavee Annurakshita[1,2,*], Minna Kellomäki[1], Vijay Singh Parihar[1,*]

[1]Biomaterials and Tissue Engineering Group, Faculty of Medicine and Health Technology, Tampere University, Finland

[2]Chemistry- School of Natural Sciences and Environmental Sciences, Newcastle University, Newcastle-Upon-Tyne, UK

*Email- shambhavee.annurakshita@tuni.fi, vijay.parihar@tuni.fi

Abstract

Extrusion-based three-dimensional (3D) printing requires biomaterial inks that combine suitable printability, rheological tunability and structural stability. Methacrylated gellan gum (GGMA) is a promising photocrosslinkable hydrogel, however, its relatively soft network can limit the structural robustness of printed constructs. The incorporation of graphene nanosheets has emerged as an effective approach to tune the rheological behaviour and polymer–nanofiller interactions of hydrogel inks. In this study, multimaterial GGMA–graphene biomaterial inks containing 0.25%, 0.5%, and 1.0% (w/w) graphene were developed and systematically evaluated. Rheological analysis demonstrated pronounced shear-thinning behaviour, yield stress, and rapid structural recovery, with graphene concentration strongly influencing flow and viscoelastic properties. *In situ* photo-rheology confirmed rapid UV-induced gelation, while oscillatory measurements and swelling studies revealed concentration-dependent changes in structural stability at intermediate graphene loadings. Printability assessment showed that biomaterial ink containing 0.5% graphene achieved the best balance among the tested formulations between filament fidelity, vertical stackability, and geometric accuracy, enabling fabrication of complex 3D constructs.

Keywords: Graphene, Gellan Gum, Multimaterials Ink, Photocrosslinking, 3D-Printing

Introduction

Three-dimensional (3D) bioprinting has emerged as a key fabrication technique in tissue engineering and regenerative medicine because it enables spatially controlled deposition of cells and biomaterials to create constructs that mimic native tissue architecture.[1–5] Several 3D bioprinting techniques have been developed for tissue engineering applications, each with distinct advantages and limitations. Extrusion-based bioprinting relies on the continuous deposition of hydrogel-based biomaterial inks through a nozzle and is well suited for processing highly viscous hydrogels and fabricating larger tissue-scale construct.[6] Jetting-based bioprinting, including inkjet and microvalve systems, enables high-speed droplet deposition with high resolution but is generally limited to low-viscosity formulations.[7] In contrast, vat photopolymerization-based techniques, such as stereolithography and digital light processing, use light-induced polymerization to achieve high spatial resolution and surface fidelity, although they require photocurable materials and are limited by optical properties such as light penetration and absorption.[8] The choice of bioprinting technique is therefore dependent on the rheological and crosslinking properties of the biomaterial ink as well as the intended application. Among available techniques, extrusion-based printing is particularly attractive due to its

View Article Online
DOI: 10.1039/D6MA00668J

compatibility with hydrogel systems, mild processing conditions and ability to fabricate complex geometries from computer-aided design models.[9] A fundamental challenge in extrusion-based printing is the development of biomaterial inks with appropriate rheological properties particularly at low polymer concentration.[10] Ideal inks must display shear-thinning behaviour to permit smooth extrusion, possess sufficient yield stress to maintain filament shape after deposition, and exhibit rapid structural recovery to preserve geometry during layer-by-layer fabrication.[11–14] Furthermore, printed construct must retain geometric fidelity following crosslinking.[15,16]

Hydrogels derived from naturally occurring polysaccharides have been widely explored as biomaterial inks due to their high-water content, and similarity to the extracellular matrix (ECM).[17,18] Gellan gum (GG), an anionic microbial polysaccharide, has attracted substantial interest due to its ability to form hydrogels under mild ionic or thermal conditions and demonstrate favourable shear-thinning behaviour for extrusion.[19] However, pristine GG hydrogels often lack sufficient mechanical strength and long-term structural stability, particularly for taller or mechanically demanding constructs, which limits their standalone use in 3D printing applications.[20,21] Chemical modification of GG with methacrylate groups yields methacrylated gellan gum (GGMA), a photocrosslinkable polymer that can form covalent networks upon exposure to light in the presence of a photoinitiator.[22] This modification enables improved control over gelation kinetics, stiffness, and post-printing stability, while preserving the ECM-like properties of the parent polymer.[23,24] GGMA is chemically modified polysaccharide hydrogel that does not contain inherent cell-adhesion motifs, which limits its direct use in cell-laden applications without additional functionalization. Despite these advantages, achieving an optimal balance between shear-responsive flow during extrusion and rapid post-deposition crosslinking remains challenging.

In addition to chemical modification strategies, the development of multicomponent or multimaterial inks have emerged as an effective approach to improve the performance of extrusion-printable hydrogels.[25,26] Single-component biomaterial inks often fail to simultaneously meet the requirements of extrusion bioprinting, including suitable rheological behaviour, structural stability, cytocompatibility, and support for cellular activity.[26,27] Consequently, combining multiple materials within a single biomaterial ink formulation has become a common strategy to achieve complementary material properties and improved printability.[28] The incorporation of 2D nanomaterials into hydrogel networks has been explored as a promising strategy to modify mechanical and rheological properties.[29–32] Among these, graphene and graphene-derived materials are particularly attractive additives due to their two-dimensional structure, high mechanical strength, large surface area, and ability to interact with polymer chains.[33–35] While numerous strategies have been explored to enhance bioink printability, including polymer blending, increased polymer content,[36] and secondary crosslinking approaches,[37–39] the use of graphene as a rheological modifier offers a complementary route to tailor printing performance without substantially altering the base hydrogel composition. When incorporated into hydrogels, graphene can modulate rheological behaviour, mechanical robustness, and swelling characteristics in a concentration-dependent manner.[34,40] However, excessive graphene content may lead to aggregation and structural heterogeneity, which can compromise printability.[41]

View Article Online
DOI: 10.1039/D6MA00668J

Building on these advances, tailoring the composition of hydrogel biomaterial inks with carefully controlled amounts of graphene offers a route to balance enhanced mechanical and functional properties with printing performance. Understanding structure interplay between graphene concentration, network structure, and resulting ink is therefore critical for designing material that support print fidelity.[42,43] However in acellular systems, such relationships are primarily relevant to extrusion stability and structural fidelity. Despite growing interest in graphene-reinforced hydrogel systems and the increasing use of GGMA as a photocrosslinkable bioink, a systematic understanding of how graphene concentration influences the rheological behaviour, gelation kinetics, and extrusion-based printability of GGMA-based systems remains limited. While previous studies have primarily focused on the mechanical reinforcement or biological functionality of graphene-containing hydrogels,[44] the coupled effects of graphene loading on structural recovery, swelling behaviour, and print fidelity in GGMA-based hydrogels have not been systematically investigated. This lack of understanding limits the rational design of nanocomposite bioinks that can balance extrusion processability with post-printing structural stability.

In this study, we develop photocrosslinkable GGMA-based biomaterial inks reinforced with varying concentrations of graphene nanosheets for extrusion-based 3D printing. Graphene was selected in this study due to its superior electrical conductivity compared to graphene oxide, making it more suitable for applications where electrically conductive scaffolds are desired. Although pristine graphene exhibits limited aqueous dispersibility, this challenge was effectively managed by using low filler concentrations within the GGMA matrix, ensuring adequate dispersion and printability. We systematically investigated rheological behaviour, viscoelastic properties, gelation kinetics, swelling, and printability, and establish a concentration-dependent relationship between nanofillers loading and extrusion performance in GGMA-based inks and evaluated the ability of these inks to generate high-fidelity constructs. The insights gained from this work provide design principles for optimizing nanocomposite hydrogel inks for extrusion-based bioprinting. Furthermore, the developed strategy may be extended to other photocrosslinkable polysaccharide-based systems. Future studies will focus on functionalized graphene derivatives and graphene oxide to further optimize the balance between electrical conductivity, dispersion stability, and cell compatibility, thereby enabling the development of multifunctional nanomaterial-reinforced bioinks for advanced tissue engineering and biofabrication applications.

Materials and Methods

Low-acyl gellan gum (GG; Gelzan™ CM, low acyl form- ~0.2%, 1000 kg/mol) was purchased from Sigma Aldrich. Methacrylic anhydride (MA), dimethyl sulfoxide (DMSO), and the photoinitiator Irgacure 2959 (I2959) were purchased from Merck KGaA (Darmstadt, Germany). Graphene nanoplatelets (Sigma-Aldrich, product no. 900407, CAS: 7782-42-5), lateral size < 2 μm and few-layer thickness, were used as received without further modification. Dialysis membranes (Spectra Por-6, molecular weight cut-off (MWCO) 3500 Da) were used for purification. Deionized (DI) water was produced using a laboratory purification system (Miele Aqua Purificator G 7795, Siemens). Dulbecco's phosphate-buffered saline (DPBS) was prepared in the lab. Proton nuclear magnetic resonance (^{1}H NMR) spectra were recorded using a spectrometer (JEOL SCZ500R Resonance, Japan)

View Article Online
DOI: 10.1039/D6MA00868J

at room temperature (RT). The dispersion and exfoliation of graphene in water were carried out using probe sonication with an UP200St ultrasonic processor (200 W, 26 kHz; Hielscher Ultrasonics, Germany). All rheological measurements were performed using a Discovery HR-2 rotational rheometer (TA Instruments Inc., USA). All reagents used were of analytical grade and used as received unless otherwise specified. All solutions were prepared with deionized (DI) water. Extrusion-based printing was performed using a multi-material 3D bioprinter (Brinter AM Technologies Oy, Finland) equipped with a pneumatically driven Pneuma Tool printhead. All experiments were performed using three parallel samples (n=3).

Synthesis of Methacrylated Gellan Gum

GGMA was prepared through the chemical modification of GG via nucleophilic substitution of hydroxyl groups on the polysaccharide backbone under mildly basic conditions (Figure 1). Initially, 2 g of GG was dispersed in 150 mL of DI water and heated to 60 °C while continuously stirred until a clear and homogeneous solution was obtained. Following complete dissolution, methacrylic anhydride (total volume 6.0 mL) was gradually introduced into the reaction mixture. The reagent was added dropwise in three equal aliquots at 30-minute intervals to facilitate controlled functionalisation and prevent excessive local concentration of the anhydride. During the reaction, the pH of the solution was carefully maintained within the range of 8–9 by periodic addition of 5 M sodium hydroxide (NaOH). The reaction mixture was maintained at 60 °C with constant stirring for 6 hours and the reaction was allowed to proceed overnight at the same temperature. After completion of the reaction, the resulting solution was transferred into dialysis tubing (molecular weight cut-off 11–14 kDa) and dialysed against DI water for five days to remove residual reagents, methacrylic acid by-products, and other low-molecular-weight impurities. The purified GGMA solution was then frozen and subjected to lyophilisation to obtain a dry, porous polymer product. The freeze-dried GGMA was stored at −20 °C until further use. The degree of methacrylation was characterised using ^{1}H NMR spectroscopy (Figure 2).

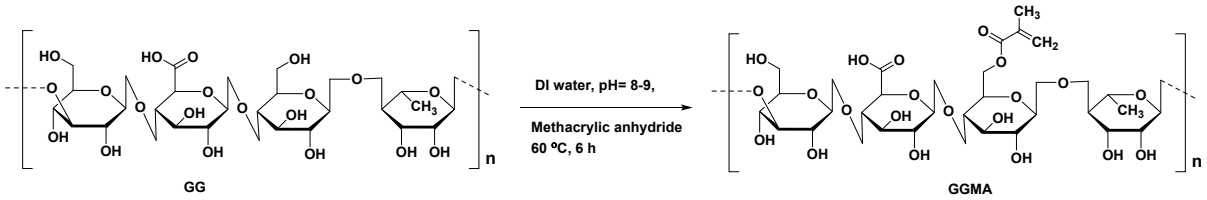

Figure 1: Synthetic routes for methacrylation of GG under basic conditions to form GGMA.

2.1 Nuclear Magnetic Resonance Spectroscopy

^{1}H NMR spectra were acquired using D_2O as solvents in 5 mm borosilicate NMR tubes. For each sample, 16 scans were collected to improve the signal-to-noise ratio of the spectra. The obtained spectra were processed using MestReNova (version 6.0.2-5475, Mestrelab Research, Spain). During processing, phase correction and baseline correction were applied to obtain clear and accurate spectra. The chemical shifts were reported in ppm and referenced to the residual solvent peak of D_2O at 4.79 ppm. Degree of substitution (DS) was determined as the amount of substituted group (MA) per one GG repeating unit as described in Equations 1.

View Article Online
DOI: 10.1039/D6MA00668J

$$DS_{MA} = \frac{Area_{6.16\ \text{ppm}} + Area_{5.71\ \text{ppm}}}{Area_{1.26\ \text{ppm}}} \cdot \frac{3}{2} \cdot 100\ \% (1)$$

Methacrylate signals at 5.71 and 6.16 ppm were integrated and DS was determined as a ratio of MA proton integrals and integral of -CH_3 signal of GG at 1.26 ppm.

2.2 Fourier Transform Infrared Spectroscopy

Fourier transform infrared (FTIR) spectroscopy was performed to identify the functional groups present in graphene, GGMA, and GGMA/graphene composite hydrogels, as well as to evaluate intermolecular interactions between the polymer matrix and graphene sheets. Spectra were collected using an attenuated total reflection (ATR) accessory mounted on a PerkinElmer Spectrum One FTIR spectrophotometer (PerkinElmer, Waltham, MA, USA). All hydrogel samples were freeze-dried and were gently ground into fine powders and pressed directly onto the diamond ATR crystal to ensure good optical contact. For graphene, the powder was evenly spread on the crystal surface and lightly compressed using the ATR pressure arm.

Preparation of Gellan Gum Methacrylate-Graphene Inks

GGMA-based inks were prepared by dissolving GGMA (1.5% w/v) in DI water containing Irgacure 2959 (0.5% w/v). Graphene was first dispersed in water and sonicated for 120 seconds to obtain a stock solution with a concentration of 5 mg mL^{-1}. The resulting graphene dispersion was then added to the GGMA polymer solution to prepare the inks, resulting in final graphene concentrations of 0.25%, 0.50%, and 1.00% (w/w) relative to GGMA. The mixtures were incubated at 37 °C for 24 hours, followed by vigorous stirring in a 40 °C water bath to ensure uniform dispersion. The use of pristine graphene nanoplatelets were selected due to their high surface area and ability to form non-covalent interactions with polysaccharide matrices without introducing additional functional groups. Prepared inks were returned to the incubator and maintained at 37 °C until further use. Visual inspection confirmed no visible aggregates prior to printing.

2.3 Rheological Characterisation

Rheological properties of GGMA and GGMA–graphene inks were evaluated using a rotational rheometer (Discovery HR-2) equipped with a parallel plate geometry (12 mm diameter, 1.5 mm gap) at RT. The analyses included shear-thinning behaviour, yield stress determination, structural recovery, *in situ* photopolymerization kinetics, and viscoelastic properties relevant to extrusion-based bioprinting.

Shear thinning and yield stress determination

Viscosity of the inks was measured over the shear rate range of 0.01–500 s^{-1} following a 300-second equilibration period. Slight material slippage or the loss at the plate periphery was observed at higher shear rates and was considered during data analysis.

Shear thinning was quantified by fitting the viscosity data to the Power-law model:

$$\mu = K\dot{\gamma}^{n-1} (2)$$

View Article Online
DOI: 10.1039/D6MA00668J

where μ represents the apparent viscosity, $\dot{\gamma}$ is the shear rate, K denotes the consistency index, and n is the flow behaviour index.[10,45,46] Linear regression of the linear region of the log (μ) vs. log ($\dot{\gamma}$) curve was used to determine the slope ($n - 1$) and the intercept log (K). Lower values of n (≤ 0.2) indicate strong shear-thinning, which facilitates smooth extrusion through the printing nozzle while promoting shape retention after deposition.[10,47]

However, the Power-law model does not incorporate the yield stress, that is, the minimum stress required to initiate the material flow, the Herschel–Bulkley model was applied. This model extends the Power-law by introducing a yield stress term:

$$\tau = \tau_0 + K\dot{\gamma}^n (3)$$

where τ is the shear stress, τ_0 is the yield stress, K and n retain their previous definitions. The shear stress vs. shear rate data were fitted using nonlinear regression to extract τ_0. The yield stress is the key parameter governing the ability of the printed structure to resist deformation and preserve geometrical integrity during and after extrusion.

Recovery behaviour

The ability of ink to recover their structure after shear-induced deformation was evaluated using a three-phase recovery test. In the first stage, a low shear rate of 0.01 s^{-1} was applied for 200 seconds to represent the quiescent state of the ink prior to extrusion. This was followed by the application of a high shear rate of 100 s^{-1} for 100 seconds, stimulating the mechanical stresses encountered during extrusion through a printing nozzle. In the final stage, the shear rate was reduced back to 0.01 s^{-1} for an additional 200 seconds to assess the extent and rate of viscosity recovery.

The percent recovery was calculated using the following formula:

$$Percent\ Recovery = \frac{\mu_{final} - \mu_{min}}{\mu_{initial} - \mu_{min}} \times (4)$$

where $\mu_{initial}$ is the mean viscosity measured during the initial low-shear phase, μ_{min} corresponds to the minimum viscosity during the high shear, and μ_{final} is the average viscosity during the recovery phase. This analysis provides insight into the ink's ability to re-establish its microstructure after extrusion and thereby retain printed geometries.

In situ photopolymerization

Gelation behaviour under UV irradiation was investigated by coupling the rheometer with an external UV curing system (BlueWave 50 spot lamp, DYMAX Corp., USA) operating at a wavelength of 365 nm and an intensity of 25 mW/cm². Prior to UV exposure, samples were soaked for 100 seconds to ensure thermal and structural stability. Rheological measurements were conducted at a constant strain of 0.1% and a frequency of 1 Hz, which are standard conditions for monitoring gelation without disrupting the forming network. This setup enabled real-time observation of the sol–gel transition, which is important for extrusion-based 3D printing applications requiring precise temporal control over photoinitiated crosslinking.

Viscoelastic properties

View Article Online
DOI: 10.1039/D6MA00668J

The viscoelastic behaviour of the hydrogels was evaluated using oscillatory amplitude and frequency sweep tests. An initial amplitude sweep was conducted over a strain range of 0.1-100% to identify the linear viscoelastic region (LVR), defined as the strain interval in which the material response remains independent of the applied deformation. During this test, the oscillation frequency was held constant at 1 Hz to approximate physiologically relevant deformation rates and to enable ensure consistent comparison between samples. The storage modulus (G′) and loss modulus (G″) were recorded as a function of strain to determine the LVR boundaries. Subsequently, frequency sweep measurements were performed within the established LVR to probe the elastic and viscous responses of the hydrogels over a range of time scales. The frequency sweep was performed over a frequency range of 0.1–100 Hz, corresponding to angular frequencies of 1–100 rad/s. A soak time of 10 seconds was applied prior to data acquisition to allow structural equilibration. These tests provide insight into the balance between solid-like and liquid-like behaviour of the hydrogels under dynamic loading conditions. All formulations were prepared from the same dissolved precursor solution; however, rheological measurements were performed sequentially, beginning with GGMA, followed by increasing the graphene concentrations (0.25%, 0.5%, and 1%). This sequential measurement approach may introduce time-dependent variations in polymer relaxation and dispersion state, which may influence crosslinking behaviour and final modulus values. Therefore, comparisons of absolute viscoelastic parameters should be interpreted as indicative of general trends rather than strict quantitative equivalence between formulations.

2.4 Printing of an Acellular Construct

GGMA and GGMA–graphene biomaterial inks were prepared following the previously established protocol and subsequently loaded into sterile 10 mL printing cartridges (Optimum syringe barrels, Nordson EFD, USA) equipped with UV-protective tapered plastic nozzles (200 μm inner diameter; SmoothFlow, Nordson EFD, USA). To ensure uniform ink consistency and remove entrapped air, the filled cartridges were incubated at 37 °C for 30 min prior to printing. Bioprinting was carried out using a multi-material extrusion-based 3D bioprinter. The cartridges were mounted onto the printhead and fitted with the corresponding nozzle, and all constructs were printed at RT with a constant nozzle movement speed of 8 mm s^{-1}. Extrusion pressure was optimized through preliminary testing to achieve stable and continuous filament deposition. Three-dimensional constructs were generated through a sequential layer-by-layer printing process. Following the deposition of each layer, rapid stabilization was achieved using an integrated UV/visible LED curing system operating at 365 nm with an intensity of 25 mW cm^{-2}. Each layer was photocrosslinked for 10 s, and a final post-curing step of 60 s was applied after printing to ensure complete crosslinking and structural integrity.

To evaluate the printability and shape fidelity, grid-like constructs (10 × 10 mm^2, two layers) were printed onto glass substrate and immediately exposed to UV light (365 nm, 25 mW/cm^2) for 120 s. Printing parameters were selected based on prior optimisation to ensure smooth filament deposition, minimise bubble formation, and achieve reproducible layer stacking and effective photocrosslinking. Printed samples were imaged using a bright-field optical microscope, and pore geometry was quantified using ImageJ software.[48]

The printability index (Pr) was calculated using the following equation:

View Article Online
DOI: 10.1039/D6MA00668J

$$Pr = \frac{L^2}{16A} (5)$$

where L represents the pore perimeter and A denotes the pore area. This dimensionless parameter reflects the roundness and fidelity of the printed pores, with $Pr \approx 1.0$ corresponding to an ideal square geometry. Values of $Pr > 1.0$ indicates excessive material deposition or over-gelation, resulting in rounded pores, whereas $Pr < 1.0$ suggests under-gelation or filament collapse.[24] To ensure reliability, at least 10 pores per sample across three independent replicates were measured. In addition to quantitative Pr, qualitative characteristics, such as filament continuity, interlayer stacking accuracy, and corner sharpness, were visually assessed.

2.5 Swelling

The swelling behaviour of GGMA and GGMA–graphene hydrogels was investigated at physiological conditions (pH 7.45, 37 °C) to evaluate their stability and responsiveness. Hydrogel samples were fabricated by dispensing the biomaterial ink formulations into 1 cm diameter syringes to obtain cylindrical constructs approximately 2 mm in height. Both GGMA and GGMA–graphene formulations were prepared at a concentration of 1.5 % (w/v). Gelation was achieved through UV-induced photocrosslinking at 365 nm with an intensity of 25 mW cm^{-2} for 2 min. Swelling experiments were performed in DPBS at 37 °C. Immediately after crosslinking, samples were gently blotted to remove surface moisture, and their initial mass was recorded (W_0). The hydrogels were then immersed in DPBS and incubated under the specified conditions. At predetermined intervals (1, 3, 6, 12 and 24 hours and subsequently at 3, 5, 7, 11, 14, 21, and 25 days), the samples were removed, lightly blotted to eliminate excess liquid, and weighed to determine the swollen mass (W□). The swelling ratio (SR) was calculated using the following equation:

$$SR = \frac{W_s - W_0}{W_s} \times (6)$$

This analysis provided insight into the hydrogel's water uptake capacity and environmental responsiveness over time. All experiments were performed in triplicate to ensure reproducibility and statistical reliability.

Results and Discussion

Synthesis and Characterization of Gellan Gum Methacrylate

GGMA was successfully synthesized as described in Section 2.1, and the resulting product was confirmed by NMR spectroscopy. The degree of substitution (DS) was determined from the NMR spectrum shown in Figure 2 using the $–CH_3$ signal at 1.26 ppm, corresponding to the methyl group of the rhamnose unit in the GG repeating structure, as an internal reference. The calculated DS was 40 ± 2%, confirming successful methacrylation.

View Article Online
DOI: 10.1039/D6MA00668J

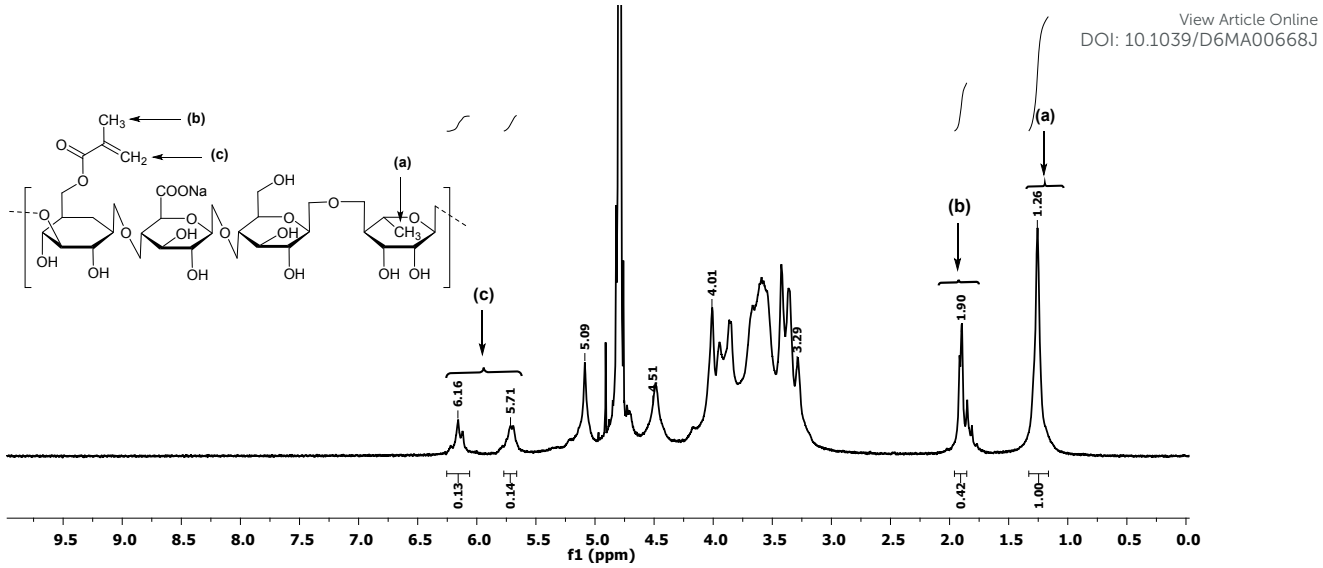

Figure 2: ^{1}H NMR spectrum of GGMA. The reference peak corresponding to the –CH_3 group of gellan gum appears at 1.26 ppm and is labeled as (a). Peaks corresponding to methacryloyl (MA) protons are observed at 1.90 ppm (b), attributed to the –CH_3 group of the MA moiety, and at 5.6 and 6.0 ppm (c), corresponding to the olefinic protons of the MA group.

The FTIR spectra of graphene, GGMA, and GGMA/graphene composite hydrogels are presented in Figure 3. GGMA exhibited characteristic absorption bands of methacrylated gellan gum, including a broad O–H stretching band at 3200–3500 cm^{-1}, C–H stretching vibrations at 2920–2950 cm^{-1}, carbonyl/carboxylate absorptions in the 1600–1730 cm^{-1} region, and C–O–C/C–O stretching bands associated with the polysaccharide backbone at 1000–1200 cm^{-1}. In contrast, graphene displayed only weak and broad features due to the limited presence of infrared-active functional groups.[49] Following graphene incorporation (0.25, 0.5, and 1 wt%), no new absorption bands were observed in the composite spectra, indicating that the addition of graphene did not alter the chemical structure of GGMA or result in the formation of new covalent bonds. Nevertheless, subtle changes were detected in several spectral regions. The broad O–H stretching band exhibited slight broadening and intensity variations with increasing graphene content, suggesting interactions between the hydroxyl groups of GGMA and the graphene surface through hydrogen bonding and interfacial adsorption. Minor changes in the shape and intensity of the carbonyl/carboxylate bands were also observed, indicating interactions between oxygen-containing functional groups of GGMA and graphene sheets. Furthermore, small intensity variations in the fingerprint region (1000–1200 cm^{-1}) suggest restricted mobility of GGMA chains resulting from their adsorption onto the graphene surface. These spectral modifications, despite the absence of significant peak shifts or new absorption bands, provide evidence of interfacial interactions between GGMA and graphene. Therefore, the FTIR results support that the graphene interacts with GGMA mainly through physical intermolecular interactions. These non-covalent interactions facilitate homogeneous graphene dispersion within the hydrogel matrix and contribute to the enhanced stability of the GGMA/graphene composite bioink.

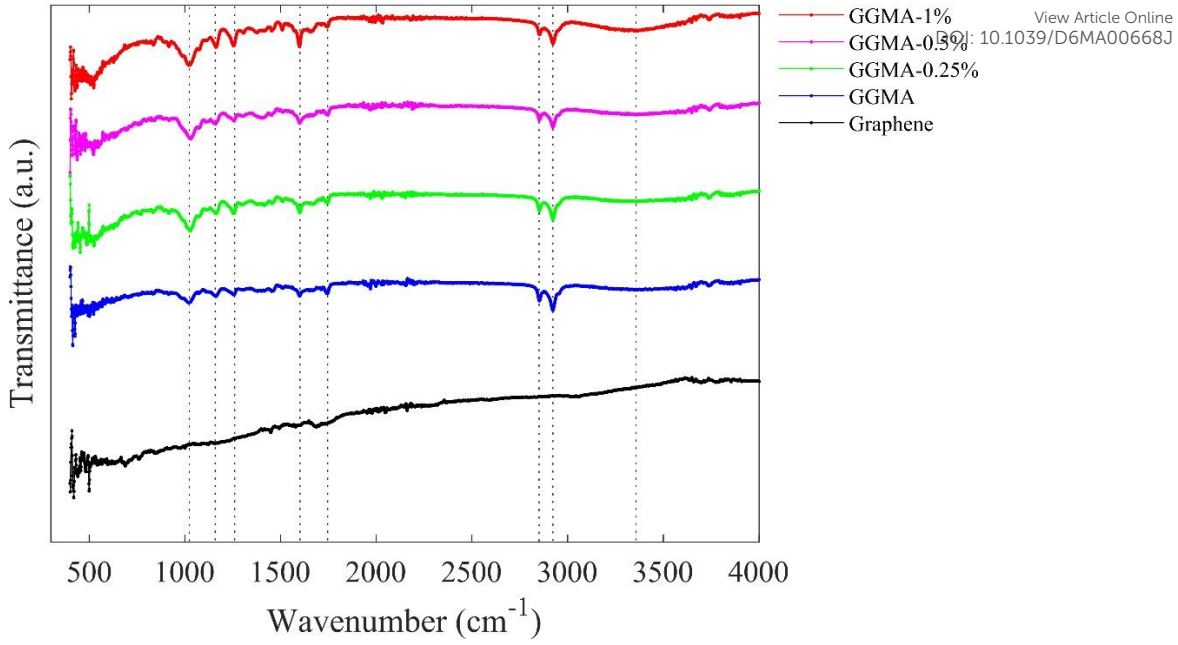

Figure 3: FTIR spectra of graphene, GGMA, and GGMA/graphene composite hydrogels showing characteristic functional groups and GGMA–graphene non-covalent interactions.

Ink Formulation and Polymer–Graphene Interactions

The GGMA–graphene inks were prepared as described in Section 2.2. Briefly, the sonicated graphene dispersion in water was added to the GGMA polymer matrix, followed by incubation and continuous stirring at 37 °C to ensure uniform mixing and dispersion of graphene within the polymer solution. As illustrated in the Figure 4, the stability of the ink is attributed to multiple intermolecular interactions between GGMA and graphene. Hydrogen bonding occurs between the oxygen-containing groups of GGMA and the graphene surface, while π–π stacking interactions and van der Waals forces may contribute to the association between the polymer chains and graphene layers.[50] These combined interactions help maintain good dispersion of graphene within the GGMA matrix, forming a stable composite bioink suitable for further processing.

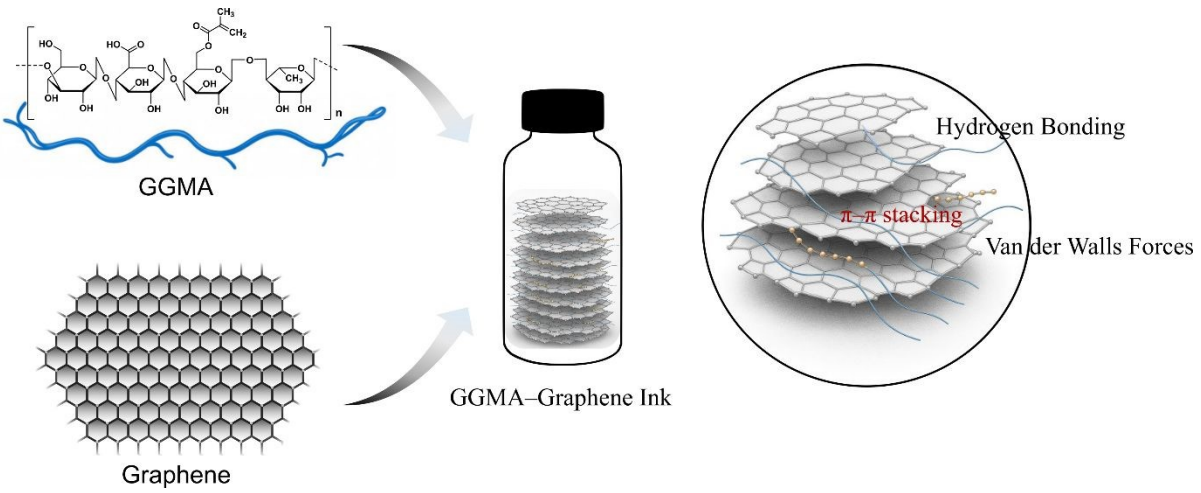

Figure 4: Schematic representation of GGMA–graphene bioink formation and the non-covalent interactions between GGMA polymer chains and graphene sheets.

View Article Online
DOI: 10.1039/D6MA00668J

The rheological characterization of GGMA and GGMA–graphene biomaterial inks (Figures 5A and 5B) reveals pronounced non-Newtonian, shear-thinning behaviour that is central to their printability performance.[51] All formulations exhibited a flow behaviour index (n) significantly less than 1, confirming strong shear-thinning properties, where viscosity decreases substantially with increasing shear rate. Low n values are widely recognized as reflective of materials with well-developed network structures that resist deformation at low shear but yield under applied stress due to reversible physical interactions such as entanglements or transient crosslinks. This shear-thinning enables efficient flow through narrow extrusion nozzles and quick recovery of structure after deposition, which is advantageous for extrusion-based printing.[52]

The consistency index (K), which quantifies the apparent viscosity at a reference shear rate, was high for GGMA (K = 146.87, indicating a robust static network at low shear. High K often correlates with greater resistance to deformation at rest, supporting the filament's ability to retain its shape after printing and resist spreading under its own weight.[12] In additive manufacturing literature, a high low-shear viscosity is associated with improved shape fidelity post-extrusion because the network structure provides elastic stiffness while permitting viscous flow only under higher shear.[12]

Incorporation of graphene at low concentration (0.25%) resulted in reduction in n (from 0.2149 to 0.1471) and a clear decrease in K (to 91.57). This suggests that even small amounts of graphene nanosheets can modify the internal network topology, weakening polymer–polymer interactions and introducing interfaces that disrupt the static network. Such disruption may increase chain mobility under shear conditions, making the material more sensitive to applied stress.[53,54] Similar effects are reported in nanocomposite systems where nanosheets at low concentration alter rheology and enhance shear thinning, often due to sheet–matrix interfacial interactions that perturb the original polymer network.[55] At higher graphene contents, lower n values (0.0504 at 0.5% and 0.0056 at 1%) were observed, indicating even stronger shear-thinning behaviour. These values imply that viscosity decreases exceptionally rapidly as shear increases, consistent with the formation of a highly stress-responsive microstructure where extensive reversible interactions are broken under shear and partially reformed when that shear is removed.[56]

The observed partial recovery in K for 0.5% (111.20) and 1% (109.83) graphene indicates that, beyond a certain filler concentration, graphene sheets begin to form additional physical contacts with GGMA chains. These interactions can create a hybrid network in which graphene not only disrupts polymer entanglements but also establishes sheet–polymer contacts that reinforce the network at rest while still yielding readily under shear. Such dual characteristics are typical in nanocomposite hydrogels when graphene sheet content crosses a threshold that favours inter-sheet contacts and network reinforcement. Graphene's influence on rheology is complex and concentration-dependent. At low concentration, nanosheets often act as rheology modifiers that disrupt existing polymer networks, reducing low-shear viscosity and increasing shear sensitivity. As concentration increases, sheets can interact more strongly with polymer chains and among themselves, forming physical clusters or percolating networks that re-enhance resistance at low shear but maintain shear-responsive behaviour.[57–59] These microstructural mechanisms have been observed in other hydrogel systems reinforced with nanomaterials where sheet-induced networks augment elasticity and yield behaviour, highlighting the role of nanostructure in dictating rheological and printing performance.[60]

View Article Online
DOI: 10.1039/D6MA00668J

The rheological trends observed in GGMA–graphene hydrogels, decreasing n with increasing graphene content and a non-monotonic trend in K, suggests that graphene nanosheets significantly modulate the interplay between network rigidity and shear-induced structural rearrangement. This behaviour can be attributed to noncovalent interactions between graphene sheets and GG chains, including hydrogen bonding, van der Waals interactions, and possible π–π or hydrophobic interactions with the polysaccharide backbone.[61] These interactions promote the formation of a transient, physically interconnected network that enhances structural integrity under low shear conditions while allowing partial disruption and alignment of polymer chains and nanosheets under applied shear. Consequently, the incorporation of graphene alters both the static viscoelastic framework and the dynamic flow response of the hydrogel matrix. Such tuneable rheological characteristics are critical for extrusion-based additive manufacturing, as they govern both printability (facilitating smooth flow through the nozzle) and print fidelity (maintaining structural stability and shape retention after deposition), highlighting the importance of optimizing nanofiller concentration to achieve balanced rheological performance.

The viscosity recovery behaviour of GGMA and GGMA–graphene ink with varying graphene concentrations was evaluated using a three-step thixotropic protocol comprising a low shear rate (0.1 s^{-1}), a high shear rate (100 s^{-1}), and a subsequent recovery phase under low shear (Figure 5C). All formulations exhibited high initial viscosities (~10^3 Pa·s), during the first low-shear interval, indicating the presence of well-developed internal networks capable of maintaining structural integrity under near static conditions. Such gel network dominance at low shear is a common characteristic of hydrogel systems with strong elastic networks and nanosheet reinforcement.[62]

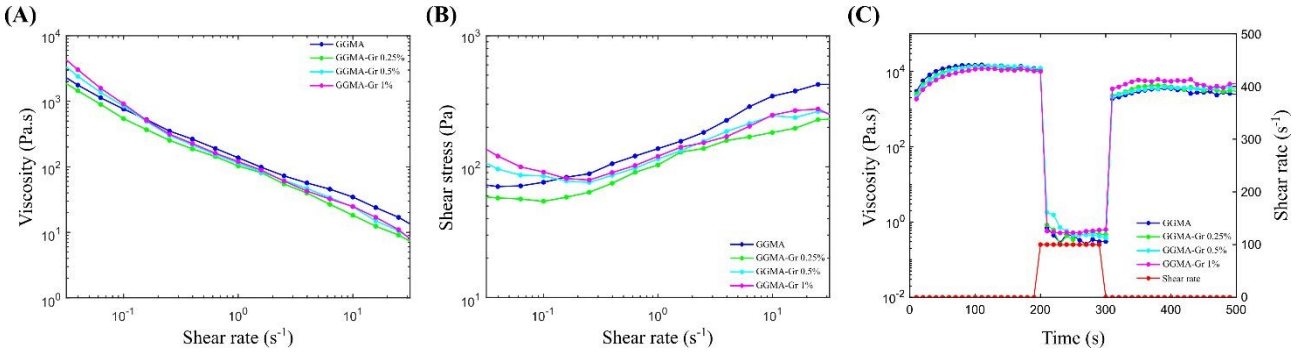

Figure 5: (A) Shear-thinning, (B) yield stress, and (C) recovery of GGMA and GGMA–graphene inks at 25 °C.

For pristine GGMA, the viscosity increased gradually during the initial low-shear period (0–200 s), reflecting time-dependent structural build-up in the absence of disruptive shear. In contrast, during the recovery phase (300–500 s), the viscosity remained relatively stable with no pronounced time-dependent increase, indicating that the majority of network reformation occurred rapidly after the removal of high shear, a behaviour also observed in nanocomposite hydrogels where reversible physical interaction restores the structure after shear cessation.[60] The similar viscosities measured at the onset of low shear (0 and 300 s) indicate the immediate recovery of the internal structure and comparable viscosities at the end of both low-shear intervals (200 s and 500 s) demonstrate reproducible recovery behaviour.

View Article Online
DOI: 10.1039/D6MA00668J

The recovery behaviour of GGMA and GGMA–graphene composites is strongly influenced by the interaction between graphene sheets and the polymer matrix. Pristine GGMA exhibited a recovery of 31.38%, reflecting limited elastic recoil due to irreversible polymer chain slippage and insufficient physical cross-linking within the matrix, consistent with observation in polymer hydrogels lacking nanoscale reinforcement.[62]

With the introduction of 0.25% graphene, the recovery increased to 35.23%, indicating that even a small amount of graphene sheets can contribute to improved recovery. At this low concentration, graphene sheets are likely to be well-dispersed within the GGMA network, where interfacial adsorption and bonding may restrict chain mobility during deformation and assist partial chain reorientation upon unloading. Similar enhancements in elasticity and mechanical response with the introduction of graphene or graphene oxide at low concentrations have been reported in polymer hydrogels, attributed to physical interactions between filler and polymer chains that effectively act as additional crosslinks.[60]

At 0.5% graphene, the recovery slightly decreased to 33.05%, suggesting that at intermediate concentrations, graphene sheets may begin to aggregate. Reduced effective interfacial area from aggregation can weaken uniform stress transfer between graphene and polymer chains. Literature on graphene-reinforced hydrogels and nanocomposite gels has noted that at moderate concentration, partial sheet aggregation can temporarily attenuate mechanical reinforcement and energy dissipation efficiency.[63]

A significant improvement in recovery was observed at 1% graphene concentration, where the recovery dramatically increased to 62.31%. At this concentration, the graphene sheets may begin to form a semi-continuous network within the GGMA matrix, which may contribute to stress distribution and provide multiple anchoring points for polymer chains. The role of graphene sheet as a physical crosslinker and elastic reinforcers in nanocomposite hydrogels has been demonstrated in studies showing increased storage modulus and resilience with higher nanosheet content, reflecting the formation of additional reversible interaction within the network.[60] These sheet-mediated interactions can suppress permanent deformation and promote elastic recoil, a key characteristic of nanocomposite hydrogel systems where physical crosslinks and sheet-induced networks contribute to strain recovery.[64]

The results indicate the critical role of graphene sheet dispersion, interfacial bonding with the polymer matrix, and concentration-dependent network formation in governing recovery behaviour. Low graphene contents provide modest reinforcement with limited recovery, intermediate concentrations may suffer from partial aggregation effects, while higher graphene concentration enables effective stress transfer and network formation, leading to a substantial enhancement in recovery performance of the GGMA–graphene composites. This concentration dependent dual behaviour from polymer network disruption at low graphene sheet concentration to reinforcement through interconnected sheet-polymer networks at higher concentration.

View Article Online
DOI: 10.1039/D6MA00668J

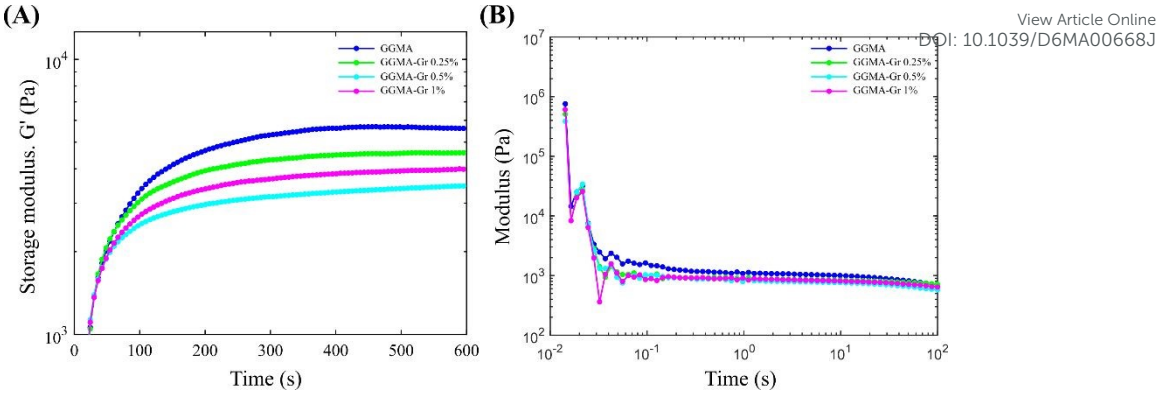

Figure 6: (A) *In situ* photocrosslinking up to 600 s and (B) Stress relaxation behaviour of GGMA and GGMA–graphene hydrogels at 5% strain over 1000 s.

The formation and mechanical evolution of GGMA and GGMA–graphene hydrogels were investigated using *in situ* photo rheology. Figure 6A shows the time-dependent evolution of the storage modulus (G′) during UV-induced crosslinking for pristine GGMA and GGMA containing 0.25%, 0.5%, and 1% graphene. Upon UV exposure, all samples exhibited a rapid increase in G′, indicating successful initiation of methacrylate polymerization and hydrogel network formation. Pristine GGMA displayed a steady rise in storage modulus, reaching a stable plateau corresponding to a mechanically robust crosslinked network. The storage modulus (G′) increased with UV irradiation time for all formulations, confirming successful photocrosslinking of the GGMA network. However, pure GGMA exhibited the highest G′, while the incorporation of graphene progressively reduced the final storage modulus. This behaviour suggests a lower degree of crosslinking in the graphene-containing hydrogels, which can be attributed to the increased opacity of the formulations. The strong UV absorption and scattering by graphene limit light penetration and photoinitiator activation,[65] resulting in reduced crosslink density and consequently lower G′ values.

The incorporation of graphene influenced the evolution and magnitude of G′ in a concentration-dependent manner. GGMA–graphene 0.25% exhibited a lower storage modulus compared to pristine GGMA throughout the crosslinking process. This reduction suggests that at low graphene content, graphene sheets may disrupt polymer chain crosslinking or interfere with photoinitiator efficiency.[64] In addition, the time elapsed between dissolution and measurement may have contributed to variations in polymer relaxation or dispersion stability, further affecting the observed modulus.

A further decrease in G′ was observed for GGMA–graphene 0.5%, which exhibited the lowest storage modulus among all formulations. This behaviour indicates that increasing graphene concentration without achieving effective network integration may exacerbate disruption of polymer–polymer crosslinking. Possible aggregation of graphene sheets at this concentration could reduce the effective interfacial area available for stress transfer, resulting in diminished mechanical performance.[66]

For GGMA–graphene 1%, a modest increase in G′ was observed relative to the 0.5% formulation, although the enhancement was not pronounced. This limited recovery in storage modulus suggests that higher graphene content begins to offset the disruptive effects observed at lower concentrations; however, the magnitude of reinforcement remains constrained. The relatively small increase in G′ may be attributed to incomplete graphene network formation, non-uniform dispersion, or time-dependent effects arising from the delayed measurement of this formulation.[67]

View Article Online
DOI: 10.1039/D6MA00668J

All samples reached a plateau in G′ at approximately 100–120 seconds after UV initiation, indicating completion of the photo crosslinking reaction and attainment of mechanical equilibrium. Based on this observation, a UV exposure time of 120 seconds was selected for all subsequent experiments to ensure consistent crosslinking conditions.

To further evaluate the viscoelastic behaviour of the crosslinked hydrogels, stress relaxation tests were performed under a constant applied strain (Figure 6B). The time-dependent modulus response of pristine GGMA and GGMA–graphene hydrogels containing 0.25%, 0.5%, and 1% graphene was monitored to assess energy dissipation and network dynamics following deformation. All formulations exhibited a characteristic stress relaxation behaviour, consisting of an initial rapid decrease in modulus followed by a more gradual decay over time. This response is typical of chemically crosslinked hydrogel networks containing reversible physical interactions, where the early-stage relaxation is associated with polymer chain rearrangement and the later-stage decay reflects constrained chain mobility within the crosslinked network.

Pristine GGMA displayed the highest initial modulus, indicating the formation of a relatively stiff network upon deformation. However, GGMA also showed a faster reduction in modulus over time, suggesting more rapid stress dissipation and limited ability to sustain applied strain. This behaviour is consistent with a densely crosslinked polymer network in which stress is relieved primarily through polymer chain relaxation.

The incorporation of graphene influenced both the initial modulus and the relaxation profile in a concentration-dependent manner. GGMA–graphene 0.25% exhibited a lower initial modulus compared to pristine GGMA, accompanied by a similar relaxation trend. The reduced modulus suggests that low graphene loading does not provide effective reinforcement and may partially disrupt polymer–polymer interactions. In addition, because rheological measurements were conducted sequentially after dissolution, time-dependent effects such as polymer relaxation and changes in dispersion state may contribute to the observed differences.

A further reduction in initial modulus was observed for GGMA–graphene 0.5%, which showed the lowest modulus across the stress relaxation experiment. This behaviour indicates that intermediate graphene concentration may interfere more strongly with network integrity, potentially due to partial aggregation of graphene sheets or reduced effective interaction with the polymer matrix, leading to enhanced viscous dissipation.

For GGMA–graphene 1%, a modest improvement in modulus retention over time was observed relative to the 0.5% formulation, although the enhancement remained limited. While the initial modulus did not exceed that of pristine GGMA, the slower decay suggests that higher graphene content may begin to restrict polymer chain mobility through additional physical interactions. Nevertheless, the relatively small magnitude of improvement indicates that graphene does not form a fully effective reinforcing framework within the hydrogel at this concentration.

These results demonstrate that graphene incorporation influences both the photo crosslinking behaviour and the viscoelastic response of GGMA hydrogels, with the mechanical performance governed by a balance between graphene–polymer interactions, graphene dispersion state, and time-dependent effects associated with sequential rheological measurements. While low to intermediate

View Article Online
DOI: 10.1039/D6MA00668J

graphene concentrations (0.25–0.5%) tend to reduce the storage modulus and promote faster stress relaxation, a higher graphene loading (1%) provides a modest improvement in stiffness retention and stress-bearing capability, although the enhancement remains limited. It is important to note that all formulations were prepared from the same precursor solution and tested sequentially, beginning with GGMA and followed by increasing graphene concentrations; therefore, the time delay between dissolution and measurement may contribute to variations in viscoelastic properties due to ongoing polymer relaxation or subtle changes in graphene dispersion. Despite this experimental constraint, consistent trends across formulations indicate that graphene concentration plays a measurable role in modulating both initial stiffness and stress dissipation. These findings underscore the importance of experimental timing when evaluating the reinforcing potential of graphene in GGMA-based hydrogel systems and highlight the complex interplay between polymer network structure, graphene content, and time-dependent effects.

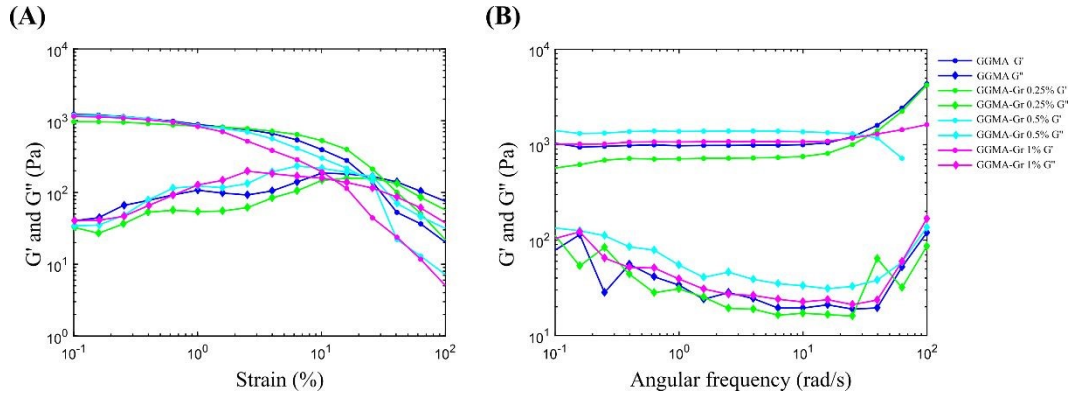

Figure 7: Viscoelastic properties of GGMA and GGMA–graphene hydrogels. (A) Storage and loss moduli obtained from amplitude sweep measurements. (B) Storage and loss moduli obtained from frequency sweep measurements.

The rheological behaviour of pristine GGMA and GGMA–graphene hydrogels with varying graphene concentrations was investigated using amplitude (Figure 7A) and frequency sweep (Figure 7B) tests to evaluate their viscoelastic properties and structural stability.

Amplitude sweep measurement showed that all hydrogel formulations exhibited a well-defined linear viscoelastic region (LVR), remaining stable up to approximately 10% strain, where the storage modulus (G′) consistently exceeded the loss modulus (G″), indicating predominantly elastic behaviour. Beyond this strain threshold, a pronounced decrease in G′ was observed, corresponding to the onset of network disruption. Among the formulations, the GGMA–graphene hydrogel containing 0.25% graphene exhibited the highest resistance to deformation, followed by pristine GGMA and the 0.5% graphene composite, which showed comparable strain tolerance. In contrast, the 1% graphene hydrogel displayed the lowest resistance to strain, suggesting limited reinforcement at this concentration.

Frequency sweep measurements further supported these observations. Across the tested frequency range, all hydrogels exhibited weak frequency dependence, with G′ remaining higher than G″, confirming the formation of stable, elastic-dominated networks. The GGMA–graphene hydrogel with 0.25% graphene consistently showed the highest G′ values, indicating enhanced network stiffness and structural integrity. Pristine GGMA and the 0.5% graphene composite displayed similar

View Article Online
DOI: 10.1039/D6MA00668J

frequency-dependent behaviour, while the 1% graphene hydrogel showed lower moduli across the frequency range. Although graphene is generally expected to reinforce hydrogel matrices,[44] no significant enhancement in storage modulus was observed with increasing graphene content. The photorheology results revealed that the degree of photocrosslinking decreased upon graphene incorporation, as evidenced by the lower G′ values obtained during UV curing. The reduced crosslink density is attributed to the strong UV absorption and scattering by graphene, which limits light penetration and consequently decreases the efficiency of photopolymerization. Since all formulations were cured under identical UV exposure conditions, the potential reinforcing effect of graphene was offset by the lower degree of network formation. As a result, the expected increase in mechanical strength arising from graphene addition was compromised by the reduced crosslinking efficiency, leading to comparable or only marginally improved storage modulus values in the composite hydrogels.

Although all samples were prepared simultaneously, slight variations in the time interval between dissolution and rheological testing may have influenced the absolute modulus values due to time-dependent structural rearrangements. However, these variations did not affect the overall trends observed in both amplitude and frequency sweep measurements.

The improved viscoelastic performance at an intermediate graphene loading (0.25%) is attributed to effective dispersion of graphene within the GGMA matrix, allowing efficient stress transfer and physical reinforcement of the hydrogel network. At higher graphene content (0.5%), partial aggregation may reduce reinforcement efficiency, while at highest content (1%), the graphene concentration appears insufficient to significantly enhance network stiffness. Notably, the combined amplitude and frequency sweep results demonstrate that graphene concentration plays a critical role in governing the viscoelastic behaviour of GGMA-based hydrogels, with 0.25% graphene providing the most favourable balance between elasticity, stiffness, and structural stability.

The swelling behaviour of GGMA and GGMA–graphene hydrogels (Figure 8) was strongly dependent on graphene concentration. Pristine GGMA exhibited the highest swelling ratio, attributed to its relatively low crosslink density and higher polymer chain mobility. Incorporation of graphene at 0.25% led to a moderate reduction in swelling, suggesting the formation of additional physical interactions between graphene sheets and the polymer network. Further increasing the graphene content to 0.5% resulted in the lowest swelling ratio and improved dimensional stability, indicating an optimal balance between network reinforcement and polymer flexibility. However, at a graphene concentration of 1%, irregular swelling behaviour and partial shrinkage were observed, likely due to graphene aggregation and possible heterogeneous crosslinking, which restricted uniform water diffusion and induced internal stresses within the hydrogel network. These results demonstrate that graphene incorporation effectively suppresses excessive swelling up to an optimal concentration, beyond which structural integrity and dimensional stability are compromised.

View Article Online
DOI: 10.1039/D6MA00668J

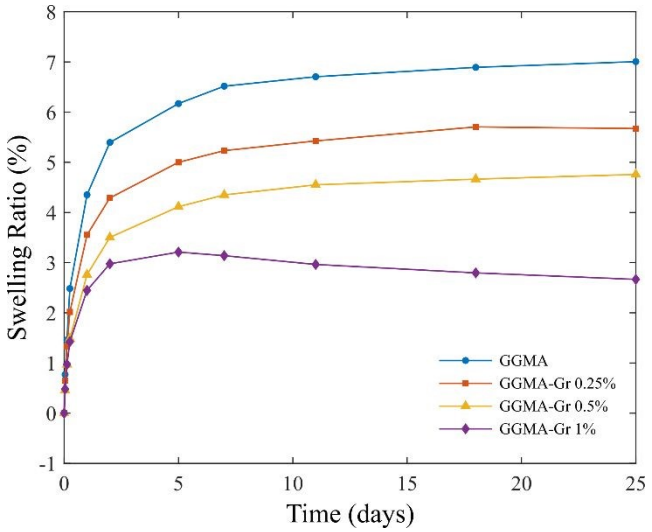

Figure 8: Time-dependent swelling behaviour of GGMA and GGMA–graphene hydrogels in DPBS (pH 7.45) at 37 °C. Data are presented as mean (n=3).

To evaluate the printability and structural fidelity of GGMA and GGMA–graphene inks, extrusion-based bioprinting was employed to fabricate constructs with increasing geometric complexity. As shown in Figures 9A, D, G, and J, all formulations were successfully printed into 2 × 2 cm grid structures consisting of six layers. These grids exhibited continuous filaments and uniform layer stacking, indicating that both GGMA and GGMA–graphene inks possess suitable viscosity and crosslinking capacity for planar constructs. Microscopic examination of the printed grids (Figures 9C, F, I, and L) revealed well-defined pore architectures and consistent filament deposition, confirming that the inks-maintained shape fidelity at finer resolutions and are therefore suitable for applications requiring precise patterning.

To further assess printability in vertically demanding geometries, cylindrical structures were fabricated (Figures 9B, E, H, and K). Among all formulations, the GGMA–graphene 0.5% ink demonstrated the best vertical printability, achieving a stable printed height of 6 mm, whereas the remaining formulations could only sustain structures up to approximately 2 mm. Based on this superior performance, the GGMA–graphene 0.5% ink was selected for printing more complex anatomical structures, including an ear and a meniscus, as shown in Figures 9M and N.

Quantitative analysis of printability supported these observations. The GGMA biomaterial ink exhibited a printability (Pr) value of 0.90, indicating near-ideal filament deposition and structural accuracy. The GGMA–Graphene 0.25% formulation showed a slightly higher Pr value of 1.03, which still reflects high print fidelity but suggests a modest reduction in structural retention, likely due to graphene-induced changes in rheological behaviour. Increasing the graphene concentration to 0.5% resulted in a Pr value of 0.96, indicating improved printability and enhanced vertical stability. However, further increasing the graphene content to 1% led to a decrease in printability (Pr = 0.89), which can be attributed to graphene sheet aggregation, nozzle clogging, and unstable extrusion during printing. Therefore, these results indicate that graphene incorporation enhances printability up to an optimal concentration, with approximately 0.5% graphene providing the best balance between structural fidelity and extrusion stability within the scope of this study.

View Article Online
DOI: 10.1039/D6MA00668J

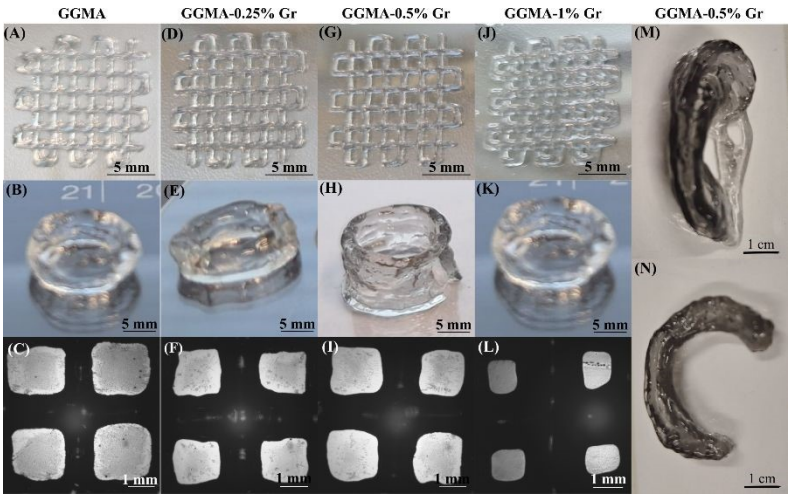

Figure 9: Extrusion-based bioprinting of six-layer grid structures and a 2 mm cylinder: (A, B) GGMA; (D, E) GGMA–graphene 0.25%; (G, H) GGMA–graphene 0.5%; (J, K) GGMA–graphene 1%. Microscopic images of the printed grids are shown in (C, F, I, and L). The optimal formulation (GGMA–graphene 0.5%) was further used to print more complex structure as shown. Ear (M) and meniscus (N) top view of the printed ear and meniscus constructs.

These results indicate that while graphene incorporation can significantly improve the printability and mechanical stability of GGMA-based biomaterial inks, excessive graphene content adversely affects flow behaviour and processability. The observed collapse or limited height in higher-concentration formulations suggests alterations in rheological or crosslinking dynamics that reduce mechanical integrity under identical printing conditions. Importantly, GGMA–graphene inks demonstrate strong potential for planar and moderately complex 3D constructs, however, further optimization such as tuning polymer concentration, crosslinking parameters may be required to reliably support taller and more intricate structures. Understanding these formulation-dependent limitations is critical for designing biomaterial inks tailored to specific 3D printing applications where vertical fidelity and mechanical robustness are essential.

Conclusion

This study presents a photocrosslinkable multimaterial ink based on GGMA reinforced with graphene for extrusion-based printing. All GGMA–graphene formulations exhibited favourable shear-thinning behaviour, viscoelastic properties, and printability, enabling the fabrication of high-resolution and structurally stable constructs. The GGMA–graphene ink is stabilized by multiple noncovalent interactions, ensuring uniform dispersion. These interactions also enable tunable rheology, supporting both printability and structural fidelity. Graphene concentration played a critical role in determining ink performance, with intermediate loading providing the best balance between flow behaviour, shape fidelity, swelling control, and vertical stability. In particular, the GGMA–graphene biomaterial ink containing 0.5% graphene demonstrated superior printability and stackability compared to other formulations. Importantly, the result demonstrate that graphene does not monotonically improve ink performance but instead exhibits the concentration dependent effect, where an optimal loading is required to balance shear-thinning behaviour, structural recovery and print fidelity. Overall, the developed GGMA–graphene biomaterial inks overcome key limitations of single-material hydrogels

View Article Online
DOI: 10.1039/D6MA00668J

and offer a promising platform for acellular extrusion-based 3D printing with improved structural fidelity and tunable printability.

Authorship Contribution

The manuscript was written through the contribution of all authors. Shambhavee Annurakshita: Conceptualization, Methodology, Investigation, Formal analysis, Data curation, Visualization, Writing – original draft, Writing – review & editing, Validation, Project administration. Minna Kellomäki: Resources, Visualization, Writing – review & editing, Project administration, Funding acquisition. Vijay Singh Parihar: Conceptualization, Methodology, Investigation, Formal analysis, Data curation, Visualization, Writing – review & editing, Validation, Supervision, Project administration. All authors have given approval for the final version of the manuscript.

Declaration of Competing Interest

The authors declare that they have no known competing financial interests or personal relationships that could have appeared to influence the work reported in this paper.

Acknowledgements

S.A. would like to thank the Jenny and Antti Wihuri Foundation and Finnish Cultural Foundation for financial support. The authors are grateful for financial support The Centre of Excellence in Body-on-Chip Research (CoEBoC) (decision #312409, #326587 and #336663) and SUSBIO PROFI7 (decision #352754), both funded by the Research Council of Finland.

Data Availability

The data supporting the findings of this study are included within the article. Additional raw data files, or data in alternative formats, are available from the corresponding author upon reasonable request.

References

1 P. S. Gungor-Ozkerim, I. Inci, Y. S. Zhang, A. Khademhosseini and M. R. Dokmeci, *Royal Society of Chemistry*, 2018, preprint, DOI: 10.1039/c7bm00765e.

2 P. Jain, H. Kathuria and N. Dubey, *Elsevier Ltd*, 2022, preprint, DOI: 10.1016/j.biomaterials.2022.121639.

3 W. Aljohani, M. W. Ullah, X. Zhang and G. Yang, *Elsevier B.V.*, 2018, preprint, DOI: 10.1016/j.ijbiomac.2017.08.171.

4 X. Sun, W. Ren, L. Xie, Q. Ren, Z. Zhu, Q. Jia, W. Jiang, Z. Jin and Y. Yu, *Virtual Phys. Prototyp.*, DOI:10.1080/17452759.2024.2384662.

5 W. L. Ng and P. Bartolo, *Mil. Med. Res.*, 2026, **13**, 100006.

6 S. Ramesh, O. L. A. Harrysson, P. K. Rao, A. Tamayol, D. R. Cormier, Y. Zhang and I. V. Rivero, *Bioprinting*, 2021, **21**, e00116.

7 W. L. Ng and V. Shkolnikov, *Biodes. Manuf.*, 2024, **7**, 771–799.

8 W. L. Ng, C. T. B. Paula, A. C. Serra, J. F. J. Coelho and P. Bartolo, *Interdisciplinary Medicine*, DOI:10.1002/inmd.70078.

9 S. V. Murphy and A. Atala, *Nature Publishing Group*, 2014, preprint, DOI: 10.1038/nbt.2958.

10 N. Paxton, W. Smolan, T. Böck, F. Melchels, J. Groll and T. Jungst, *Biofabrication*, DOI:10.1088/1758-5090/aa8dd8.

11 A. Martorana, G. Pitarresi, F. S. Palumbo, G. Barberi, C. Fiorica and G. Giammona, *Polymers (Basel).*, DOI:10.3390/polym14091844.

12 A. Schwab, R. Levato, M. D'Este, S. Piluso, D. Eglin and J. Malda, *American Chemical Society*, 2020, preprint, DOI: 10.1021/acs.chemrev.0c00084.

13 G. J. Gillispie, J. Copus, M. Uzun-Per, J. J. Yoo, A. Atala, M. K. K. Niazi and S. J. Lee, *Mater. Des.*, DOI:10.1016/j.matdes.2023.112237.

14 P. A. Amorim, M. A. d'Ávila, R. Anand, P. Moldenaers, P. Van Puyvelde and V. Bloemen, *Elsevier B.V.*, 2021, preprint, DOI: 10.1016/j.bprint.2021.e00129.

15 Y. J. Shin, R. T. Shafranek, J. H. Tsui, J. Walcott, A. Nelson and D. H. Kim, *Acta Biomater.*, 2021, **119**, 75–88.

16 H. Chu, K. Zhang, Z. Rao, P. Song, Z. Lin, J. Zhou, L. Yang, D. Quan and Y. Bai, *Biomaterials Translational*, 2023, **4**, 115–127.

17 M. C. Teixeira, N. S. Lameirinhas, J. P. F. Carvalho, A. J. D. Silvestre, C. Vilela and C. S. R. Freire, *Int. J. Mol. Sci.*, DOI:10.3390/ijms23126564.

18 S. Heid and A. R. Boccaccini, *Acta Materialia Inc*, 2020, preprint, DOI: 10.1016/j.actbio.2020.06.040.

19 Z. Xu, Z. Li, S. Jiang and K. M. Bratlie, *ACS Omega*, 2018, **3**, 6998–7007.

20 M. Sahranavard, A. Zamanian, A. B. Ghader and M. Shahrezaee, *Int. J. Biol. Macromol.*, DOI:10.1016/j.ijbiomac.2025.145800.

21 M. Aghajani, H. R. Garshasbi, S. M. Naghib and M. R. Mozafari, *Multidisciplinary Digital Publishing Institute (MDPI)*, 2025, preprint, DOI: 10.3390/biomedicines13030731.

22 S. Pacelli, P. Paolicelli, I. Dreesen, S. Kobayashi, A. Vitalone and M. A. Casadei, *Int. J. Biol. Macromol.*, 2015, **72**, 1335–1342.

23 U. D'Amora, A. Ronca, S. Scialla, A. Soriente, P. Manini, J. W. Phua, C. Ottenheim, A. Pezzella, G. Calabrese, M. G. Raucci and L. Ambrosio, *Nanomaterials*, DOI:10.3390/nano13040772.

24 H. Jongprasitkul, S. Turunen, V. S. Parihar and M. Kellomäki, *Bioprinting*, DOI:10.1016/j.bprint.2021.e00185.

25 X. Cui, J. Li, Y. Hartanto, M. Durham, J. Tang, H. Zhang, G. Hooper, K. Lim and T. Woodfield, *Wiley-VCH Verlag*, 2020, preprint, DOI: 10.1002/adhm.201901648.

26 I. C. P. Rodrigues, L. C. Orrantia Clark, X. Kuang, R. Sanchez Flores, É. S. N. Lopes, L. P. Gabriel and Y. S. Zhang, *Compos. B Eng.*, DOI:10.1016/j.compositesb.2024.111337.

27 J. Gopinathan and I. Noh, *BioMed Central Ltd.*, 2018, preprint, DOI: 10.1186/s40824-018-0122-1.

View Article Online
DOI: 10.1039/D6MA00668J

28 Y. Cai, S. Y. Chang, S. W. Gan, S. Ma, W. F. Lu and C. C. Yen, *Acta Materialia Inc*, 2022, preprint, DOI: 10.1016/j.actbio.2022.08.014.

29 X. Yan, H. Huang, A. M. Bakry, W. Wu, X. Liu and F. Liu, *Elsevier B.V.*, 2024, preprint, DOI: 10.1016/j.ijbiomac.2024.132583.

30 A. Chakraborty, A. Roy, S. P. Ravi and A. Paul, *Royal Society of Chemistry*, 2021, preprint, DOI: 10.1039/d1bm00605c.

31 H. Rastin, N. Mansouri, T. T. Tung, K. Hassan, A. Mazinani, M. Ramezanpour, P. L. Yap, L. Yu, S. Vreugde and D. Losic, *John Wiley and Sons Inc*, 2021, preprint, DOI: 10.1002/adhm.202101439.

32 B. Gaihre, M. A. Potes, V. Serdiuk, M. Tilton, X. Liu and L. Lu, *Elsevier Ltd*, 2022, preprint, DOI: 10.1016/j.biomaterials.2022.121507.

33 Z. Wang, H. Guo, J. Zhang, Y. Qian and Y. Liu, *Multidisciplinary Digital Publishing Institute (MDPI)*, 2024, preprint, DOI: 10.3390/lubricants12050149.

34 A. Madhusudhan, T. A. Suhagia, C. Sharma, S. K. Jaganathan and S. D. Purohit, *Multidisciplinary Digital Publishing Institute (MDPI)*, 2024, preprint, DOI: 10.3390/polym16233318.

35 K. Deshmukh, T. Kovářík, M. Pandey, P. Rani, V. D. Punetha, S. K. K. Pasha and K. K. Sadasivuni, *Elsevier Ltd*, 2026, preprint, DOI: 10.1016/j.mtsust.2025.101256.

36 X. B. Chen, A. Fazel Anvari-Yazdi, X. Duan, A. Zimmerling, R. Gharraei, N. K. Sharma, S. Sweilem and L. Ning, *Bioact. Mater.*, 2023, **28**, 511–536.

37 H. Jongprasitkul, S. Turunen, M. Kellomäki and V. S. Parihar, *Mater. Adv.*, 2024, **5**, 5823–5837.

38 H. Jongprasitkul, S. Turunen, D. A. Fulton, M. Kellomäki and V. S. Parihar, *Bioprinting*, 2025, **50**, e00432.

39 H. Jongprasitkul, S. Turunen, V. S. Parihar and M. Kellomäki, *Biomacromolecules*, 2023, **24**, 502–514.

40 D. Moura, R. F. Pereira and I. C. Gonçalves, *Elsevier Ltd*, 2022, preprint, DOI: 10.1016/j.mtchem.2021.100617.

41 J. Li, X. Liu, J. M. Crook and G. G. Wallace, *Elsevier Ltd*, 2019, preprint, DOI: 10.1016/j.mtchem.2019.100199.

42 M. K. Goshisht, A. Goshisht, A. Bajpai and A. Bajpai, *Royal Society of Chemistry*, 2025, preprint, DOI: 10.1039/d5pm00137d.

43 J. Lai, X. Chen, H. H. Lu and M. Wang, *3D Print. Addit. Manuf.*, 2024, **11**, e2022–e2032.

44 S. Hussain and S. S. Maktedar, *Results Chem.*, 2023, **6**, 101029.

45 Md. Sarker and X. B. Chen, *J. Manuf. Sci. Eng.*, DOI:10.1115/1.4036226.

46 C. W. . Macosko, *Rheology : principles, measurements, and applications*, VCH, 1994.

47 E. Reina-Romo, S. Mandal, P. Amorim, V. Bloemen, E. Ferraris and L. Geris, *Front. Bioeng. Biotechnol.*, DOI:10.3389/fbioe.2021.701778.

48 J. Schindelin, I. Arganda-Carreras, E. Frise, V. Kaynig, M. Longair, T. Pietzsch, S. Preibisch, C. Rueden, S. Saalfeld, B. Schmid, J. Y. Tinevez, D. J. White, V. Hartenstein, K. Eliceiri, P. Tomancak and A. Cardona, 2012, preprint, DOI: 10.1038/nmeth.2019.

49 T. Alves, W. S. Mota, C. Barros, D. Almeida, D. Komatsu, A. Zielinska, J. C. Cardoso, P. Severino, E. B. Souto and M. V. Chaud, *J. Mater. Sci.*, 2024, **59**, 14948–14980.

50 S. Pan, P. Wang, P. Liu, T. Wu, Y. Liu, J. Ma and H. Lu, *J. Mater. Chem. C Mater.*, 2021, **9**, 5779–5788.

51 P. N. Dave, P. M. Macwan, B. Kamaliya and A. Kumar, *Journal of Materials Science: Materials in Engineering*, DOI:10.1186/s40712-024-00148-w.

52 M. I. Calafel, M. Criado-Gonzalez, R. Aguirresarobe, M. Fernández and C. Mijangos, *Royal Society of Chemistry*, 2025, preprint, DOI: 10.1039/d5ma00019j.

53 M. P. Weir, D. W. Johnson, S. C. Boothroyd, R. C. Savage, R. L. Thompson, S. M. King, S. E. Rogers, K. S. Coleman and N. Clarke, *ACS Macro Lett.*, 2016, **5**, 430–434.

54 P. Govindaraj, A. Sokolova, N. Salim, S. Juodkazis, F. K. Fuss, B. Fox and N. Hameed, *Elsevier Ltd*, 2021, preprint, DOI: 10.1016/j.compositesb.2021.109353.

55 M. Sabzi, L. Jiang and N. Nikfarjam, *Ind. Eng. Chem. Res.*, 2015, **54**, 8175–8182.

56 R. Kotsilkova and S. Tabakova, *Nanomaterials*, DOI:10.3390/nano13050835.

57 K. P. M. Lee, M. Brandt, R. Shanks and F. Daver, *Polymers (Basel).*, 2020, **12**, 1–15.

58 M. Namvari, L. Du and F. J. Stadler, *RSC Adv.*, 2017, **7**, 21531–21540.

59 C. Vallés, R. J. Young, D. J. Lomax and I. A. Kinloch, *J. Mater. Sci.*, 2014, **49**, 6311–6320.

60 A. El-Refaey, Y. Ito and M. Kawamoto, *Nanomaterials*, DOI:10.3390/nano12183129.

61 H. Kim, A. A. Abdala and C. W. MacOsko, 2010, preprint, DOI: 10.1021/ma100572e.

62 S. Pacelli, P. Paolicelli, I. Dreesen, S. Kobayashi, A. Vitalone and M. A. Casadei, *Int. J. Biol. Macromol.*, 2015, **72**, 1335–1342.

63 P. N. Dave, P. M. Macwan and B. Kamaliya, *Mater. Adv.*, 2023, **4**, 2971–2980.

64 S. Tarashi, H. Nazockdast and G. Sodeifian, *Polymer (Guildf).*, DOI:10.1016/j.polymer.2019.121837.

65 Z. Hang, H. Yu, Y. Lu, X. Huai and L. Luo, *Materials*, 2019, **13**, 153.

66 A. Farshidfar, S. Bazgir, A. A. Katbab and A. Vaziri, *Polym. Test.*, DOI:10.1016/j.polymertesting.2023.107951.

67 D. G. Papageorgiou, Z. Li, M. Liu, I. A. Kinloch and R. J. Young, *Royal Society of Chemistry*, 2020, preprint, DOI: 10.1039/c9nr06952f.

View Article Online
DOI: 10.1039/D6MA00668J

Data availability statements

Data will be made available upon reasonable request. The datasets generated and/or analyzed during this study will be available in the Trepo, the institutional repository of Tampere University (https://trepo.tuni.fi/).